applied optics

Automatic initial configuration in off-axis reflective optical system design using combined nodal and Seidel aberration

Zheng Qu,[1] Xing Zhong,[1,2,3,*] Kun Zhang,[4] Lei Li,[1] and Yuanhang Wang[1]

[1]Changchun Institute of Optics, Fine Mechanics and Physics, Chinese Academy of Sciences, Changchun, 130033, China
[2]Chang Guang Satellite Technology Co., Ltd., Changchun, 130102, China
[3]Key Laboratory of Advanced Technology for Aerospace Vehicles of Liaoning Province, Dalian University of Technology, Dalian, 116024, China
[4]Institute of Optics and Electronics, Chinese Academy of Sciences, Chengdu, 610209, China
*Corresponding author: ciomper@163.com

Received 25 February 2022; revised 22 March 2022; accepted 28 March 2022; posted 4 April 2022; published 21 April 2022

Currently, an off-axis reflective optical system is designed always from a coaxial initial system, and good imaging performance depends heavily on the choice of good initial configurations. This paper first establishes an imaging-performance evaluation function of the off-axis initial configuration based on nodal aberration theory and Seidel aberration theory. An automatic optimization method of the off-axis initial configuration using the global simulated annealing algorithm is proposed. Two design examples of off-axis three-mirror reflective optical systems are used to demonstrate the effectiveness and simplicity based on the initial configuration design method. Example 1: a series of optical systems with a large 10° × 3° field of view (FOV) is quickly and simply implemented using simple surfaces, and the optical systems exhibit perfect imaging quality. Example 2: starting from the good automatic initial configurations, two larger 20° × 3° FOV optical systems with focal lengths of 500 mm and f-numbers of five are designed, resulting in good imaging performance and providing a valuable design reference.

https://doi.org/10.1364/AO.457092

1. INTRODUCTION

Reflective optical systems are applied for various fields such as astronomical telescopes, optical remote sensing, lithography, microscopy, thermal imaging systems, etc. These applications come from the merits of high imaging performance, good thermal performance, no chromatic aberration, wide observation spectrum range, compact volume, etc. [1–7]. Reflective optical systems are generally designed by creating a suitable initial system and then optimizing it with optical design software. Especially, a good initial configuration is crucial, which determines the ease of subsequent optimization [8–10].

With the rapid development of processing and inspection technology, reflective optical systems are developing toward large apertures, long focal lengths, and large fields of view (FOV); however, simple spherical and aspheric surfaces have low degrees of design freedom, and it is difficult to achieve higher design requirements while also correcting the unconventional aberrations induced by breaking of the rotational symmetry. To overcome these problems, freeform optical surfaces, which can be characterized as non-rotationally symmetric surfaces, have been introduced into optical design and have been used successfully in several areas. These surfaces can correct the aberrations that occur in non-rotationally symmetric systems well and thus help to achieve better imaging performance, improved system parameters, more compact system configuration, and fewer elements [11–15]. However, there are certain difficulties in engineering implementation. Optical systems with large FOVs are very valuable in using simple surfaces while maintaining a compact volume, which is closely related to the design method of the optical system.

Various optical system design methods have emerged. More and more methods focus on automatic design and the complexity of the design. At the same time, relative optimization algorithms have emerged, such as the genetic algorithm (GA) [16,17], particle swarm algorithm (PSA) [18], simulated annealing algorithm (SA) [19], and deep learning [20]. However, comparing the traditional damped-least-squares (DLS) method, the SA method as a global optimization algorithm is better at solving the possible local minimum problem for calculation of the evaluation function. In this paper, the SA can be realized to optimize initial structures. Although these above-mentioned methods can obtain imaging quality very well by a simple design process, they often ignore the issues of surface complexity and corresponding processing difficulty, and manufacturing costs are getting higher as using more freeform. Therefore, the use of simpler surfaces to achieve image

quality requirements to save manufacturing costs, through the complete system design process in this paper, helps reduce the difficulty and cost of optical system construction. It is an important reference value for the development of aerospace optical payloads.

This paper investigates an automatic initial configuration design method based on nodal aberration theory (NAT) and Seidel aberration theory (SAT) for the large FOV reflective optical system. The contributions can be summarized as follows: first, pupil off-axis NAT is derived by introducing the off-axis parameters and combining NAT with SAT to establish the evaluation function of imaging performance. Here, the relationship between off-axis primary aberration and initial structure parameters is linked. The pupil off-axis coefficients are rewritten and transform the vector into scalar values for evaluation function calculation. Second, the evaluation function is established based on the rewritten off-axis aberration coefficients and relative constraints, and the weight assigned to each aberration coefficient is adjusted according to the actual algorithm simulated results. Third, a global SA is used to calculate the evaluation function and get the optimal solutions given the boundaries of the nonlinear system structure variables. These initial parameters can be output by Python and easily get access with ZOS-API in Zemax. The success rate of SA is investigated by the first 10 trials in pursuing effective optimization. Finally, two design examples are simulated for demonstrating the feasibility of the initial configuration automatic design method. Example 1: a series of off-axis reflective optical systems with a $10° \times 3°$ FOV is designed by using the automatic initial configuration design method. The surfaces of these large $10° \times 3°$ FOV reflective systems are all simple aspherical, and they need only one step of optical software optimization to obtain it, which solves the possibility of getting stuck in locally optimal solutions. Example 2: from the perfect automatic initial configurations, two $20° \times 3°$ FOV off-axis reflective optical systems are achieved with simple surfaces. The purpose is further to prove the flexibility and simplicity of the theory and design method. These systems supply good references for the design of other kinds of reflective systems.

2. OFF-AXIS REFLECTIVE OPTICAL SYSTEM DESIGN METHOD

A. Pupil Off-Axis Nodal Aberration Theory

NAT is already a very well-established theory to describe the primary aberrations of rotationally symmetric optical systems. The symmetry NAT was earlier derived from the scalar to the vector expression, and the primary wave aberration is shown as [21]

$$\begin{aligned} \mathrm{W} &= \mathrm{W}_{040}(\vec{\rho}\cdot\vec{\rho})^2 + \mathrm{W}_{131}(\vec{H}\cdot\vec{\rho})(\vec{\rho}\cdot\vec{\rho}) + \mathrm{W}_{222}(\vec{H}\cdot\vec{\rho})^2 \\ &\cdots + \mathrm{W}_{220}(\vec{H}\cdot\vec{H})(\vec{\rho}\cdot\vec{\rho}) + \mathrm{W}_{311}(\vec{H}\cdot\vec{H})(\vec{H}\cdot\vec{\rho}), \end{aligned} \tag{1}$$

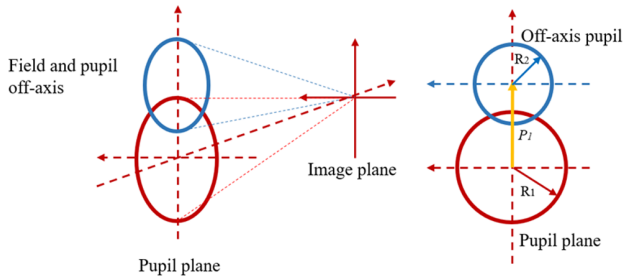

Fig. 1. Schematic representation of off-axis pupil.

where W_{040}, W_{131}, W_{222}, W_{220}, and W_{311} are the primary wave aberration coefficients of a coaxial optical system, $\vec{H}$ is the normalized field vector, and $\vec{\rho}$ is the normalized aperture vector.

Therefore, the primary wave aberration of coaxial optical systems can be summarized as

$$\begin{cases} \mathrm{W} = \sum\limits_j \mathrm{W}_{040j}\left(\overrightarrow{\rho_1}\cdot\overrightarrow{\rho_1}\right)^2 + \sum\limits_j \mathrm{W}_{131j}\left(\vec{H}\cdot\overrightarrow{\rho_1}\right)\left(\overrightarrow{\rho_1}\cdot\overrightarrow{\rho_1}\right) + \frac{1}{2}\sum\limits_j \mathrm{W}_{222j}\vec{H}^2\cdot\overrightarrow{\rho_1}^2 \\ \cdots + \sum\limits_j \mathrm{W}_{220mj}(\vec{H}\cdot\vec{H})\left(\overrightarrow{\rho_1}\cdot\overrightarrow{\rho_1}\right) + \sum\limits_j \mathrm{W}_{311j}(\vec{H}\cdot\vec{H})\left(\vec{H}\cdot\overrightarrow{\rho_1}\right), \\ \mathrm{W}_{220mj} = \mathrm{W}_{220j} + \frac{1}{2}\mathrm{W}_{222j} \end{cases}, \tag{2}$$

where j is the optical surface order, and $\overrightarrow{\rho_1}$ is a coaxial normalized aperture vector modified to distinguish the off-axis $\overrightarrow{\rho_2}$.

For off-axis optical systems, the lack of a common rotationally symmetric axis makes the configuration more complicated than conventional coaxial ones because of the emerging off-axis aberration. To adress this difficulty, two important pupil off-axis parameters are introduced including the pupil off-center vector $\overrightarrow{P_1}$ and pupil scaling parameter M, which easily show the difference between pupil off axis and on axis. The pupil off-axis principle shown in Fig. 1, and the relationship after adding the off-axis parameters can be described as

$$M = \frac{R_2}{R_1},\ \overrightarrow{P_2} = \frac{\overrightarrow{P_1}}{R_1},\ \overrightarrow{\rho_1} = M\rho_2 + \overrightarrow{P_2}, \tag{3}$$

where R_1 and R_2 are the apertures radius of before and after pupil descent, respectively.

Then, the pupil off-axis NAT is derived by adding the off-axis parameters; it is worth noting that the operations need to satisfy the following rules:

$$2(\vec{A}\cdot\vec{B})(\vec{A}\cdot\vec{C}) = (\vec{A}\cdot\vec{A})(\vec{B}\cdot\vec{C}) + \vec{A}^2\cdot\overrightarrow{BC}, \tag{4}$$

$$\vec{A}\cdot\overrightarrow{BC} = \vec{A}\vec{B}^*\cdot\vec{C}. \tag{5}$$

Therefore, the pupil off-axis NAT can be derived from the symmetry NAT for several optical surfaces as

$$
\begin{aligned}
\mathrm{W} = {} & M^4 \sum_j \mathrm{W}_{040j} (\vec{\rho}_2 \cdot \vec{\rho}_2)^2 + M^3 \left(4 \sum_j \mathrm{W}_{040j} \overrightarrow{P_2} + \sum_j \mathrm{W}_{131j} \vec{H} \right) \cdot \overrightarrow{\rho_2} \left(\overrightarrow{\rho_2} \cdot \overrightarrow{\rho_2} \right) \\
& \cdots + M^2 \left(2 \sum_j \mathrm{W}_{040j} \overrightarrow{P_2}^2 + \sum_j W_{131j} \overrightarrow{P_2} \cdot \vec{H} + \tfrac{1}{2} \sum_j \mathrm{W}_{222j} \vec{H}^2 \right) \cdot \overrightarrow{\rho_2}^2 \\
& \cdots + M \left(4 \sum_j \mathrm{W}_{040j} \left(\overrightarrow{P_2} \cdot \overrightarrow{P_2} \right) \overrightarrow{P_2} + 2 \sum_j W_{131j} \left(\overrightarrow{P_2} \cdot \overrightarrow{P_2} \right) \vec{H} + \sum_j W_{131j} \overrightarrow{P_2} \right) \cdot \overrightarrow{\rho_2} \left(\overrightarrow{\rho_2} \cdot \overrightarrow{\rho_2} \right) \\
& \cdots + M^2 \left(4 \sum_j W_{040j} \left(\overrightarrow{P_2} \cdot \overrightarrow{P_2} \right) + \sum_j \mathrm{W}_{131j} \left(\overrightarrow{P_2} \cdot \vec{H} \right) + \sum_j \mathrm{W}_{220mj} (\vec{H} \cdot \vec{H}) \right) \\
& \cdots + M \left(\sum_j \mathrm{W}_{222j} \vec{H}^2 \cdot \overrightarrow{P_2}^* + 2 \sum_j \mathrm{W}_{220Mj} (\vec{H} \cdot \vec{H}) \overrightarrow{P_2} + \sum_j \mathrm{W}_{131j} (\vec{H} \cdot \vec{H}) \vec{H} \right) \cdot \overrightarrow{\rho_2}.
\end{aligned} \tag{6}
$$

For the pupil off-axis NAT, the wave aberration coefficients are still the same as the coaxial system, which can be related to Seidel primary aberration coefficients. Because the off-axis NAT is derived by adding only characteristic parameters, the coaxial aberration coefficients are used for the off-axis NAT coefficients. The relationship between off-axis NAT and SAT is established in the following section, and an imaging performance evaluation function with initial optical configuration parameters as variables is also generated.

B. Establishing Evaluation Function Combining Seidel Aberration Theory

For the symmetric coaxial optical system, SAT is often useful to calculate the initial structures; however, it is still difficult to get good imaging performance by enlarging the FOV step by step using DLS. This method can be achieved based on rich experiments in optical design and has a very high possibility to be trapped in a local minimum. Thus, this paper concentrates on establishing an evaluation function related to the primary off-axis aberration coefficients and investigates a relationship between aberration and configuration parameters, which is a basis for further global optimization. NAT is linked to SAT analysis from the relationship between the primary wave aberration coefficients and geometric aberration coefficients. The relationship between primary wave aberration coefficients and Seidel aberration coefficients is [14]

$$
\mathrm{W}_{040j} = \frac{1}{8} S_{\mathrm{I}j}, \ \mathrm{W}_{131j} = \frac{1}{2} S_{\mathrm{II}j}, \ \mathrm{W}_{222j} = \frac{1}{2} S_{\mathrm{III}j},
$$

$$
\mathrm{W}_{220j} = \frac{1}{4} S_{\mathrm{IV}j}, \ \mathrm{W}_{311j} = \frac{1}{2} S_{\mathrm{V}j}, \tag{7}
$$

where $S_{\mathrm{I}j}$, $S_{\mathrm{II}j}$, $S_{\mathrm{III}j}$, $S_{\mathrm{IV}j}$, and $S_{\mathrm{V}j}$ are the third-order Seidel aberration coefficients of spherical, coma, astigmatism, field curvature, and distortion, respectively.

The theory is applicable to off-axis two-mirror, three-mirror, and four-mirror reflective optical systems. In this paper, the off-axis three-mirror optical system is designed for demonstrating the feasibility of the theory. The paraxial axis approximation for geometrical optics has been very widely applied [22], and the derivation of the three-mirror reflective optical system has been confirmed [16], so a detailed derivation is not carried out in this paper. In this paper, a three-mirror off-axis optical system can be realized to demonstrate the whole idea and method. The three-mirror system is composed of three mirrors: a primary mirror (PM), secondary mirror (SM), and tertiary mirror (TM). The third-order Seidel aberration coefficients are given by the following expressions [22]:

$$
\begin{cases}
S_{\mathrm{I}} = \frac{1}{4} \left[(k_1 - 1) \beta_1{}^3 \beta_2{}^3 - k_2 \alpha_1 \beta_2{}^3 (1 + \beta_1)^3 + k_3 \alpha_1 \alpha_2 (1 + \beta_2)^3 + \alpha_1 \beta_2{}^3 (1 + \beta_1)(1 - \beta_1)^2 \right. \\
\cdots - \left. \alpha_1 \alpha_2 (1 + \beta_2)(1 - \beta_2)^2 \right], \\
S_{\mathrm{II}} = -\frac{k_2 (\alpha_1 - 1) \beta_2^3 (1 + \beta_1)^3}{4 \beta_1 \beta_2} - \frac{[\alpha_2 (\alpha_1 - 1) + \beta_1 (1 - \alpha_2)](1 + \beta_2)(1 - \beta_2)^2}{4 \beta_1 \beta_2} \\
\ldots + k_3 \frac{[\alpha_2 (\alpha_1 - 1) + \beta_1 (1 - \alpha_2)](1 + \beta_2)^3}{4 \beta_1 \beta_2} + \frac{(\alpha_1 - 1) \beta_2^3 (1 + \beta_1)(1 - \beta_1)^2}{4 \beta_1 \beta_2} - \frac{1}{2}, \\
S_{\mathrm{III}} = -k_2 \frac{\beta_2 (\alpha_1 - 1)^2 (1 - \beta_1)^3}{4 \alpha_1 \beta_1^2} - \frac{[\alpha_2 (\alpha_1 - 1) + \beta_1 (1 - \alpha_2)]^2 (1 + \beta_2)(1 - \beta_2)^2}{4 \alpha_1 \alpha_2 \beta_1^2 \beta_2^2} \\
\cdots - \frac{[\alpha_2 (\alpha_1 - 1) + \beta_1 (1 - \alpha_2)](1 - \beta_2)(1 + \beta_2)}{\alpha_1 \alpha_2 \beta_1 \beta_2} + \frac{\beta_2 (1 + \beta_1)}{\alpha_1} + \frac{1 + \beta_2}{\alpha_1 \alpha_2} - \beta_1 \beta_2 \\
\cdots + \frac{k_3 [\alpha_2 (\alpha_1 - 1) + \beta_1 (1 - \alpha_2)]^2 (1 + \beta_2)^3}{4 \alpha_1 \alpha_2 \beta_1^2 \beta_2^2} + \frac{\beta_2 (\alpha_2 - 1)^2 (1 + \beta_1)(1 - \beta_1)^2}{4 \alpha_1 \beta_1^2} \\
\cdots - \frac{\beta_2 (\alpha_2 - 1)(1 + \beta_1)(1 - \beta_1)}{\alpha_1 \beta_1}, \\
S_{\mathrm{IV}} = \beta_1 \beta_2 - \frac{\beta_2 (1 + \beta_1)}{\alpha_1} + \frac{1 + \beta_2}{\alpha_1 \alpha_2} \\
S_{\mathrm{V}} = \frac{2 (\alpha_1 - 1)(1 + \beta_1)}{\alpha_1^2 \beta_1} + \frac{(1 + \beta_1)(\alpha_1 - 1)^3 (\beta_1 - 1)^2}{4 \alpha_1^2 \beta_1{}^3} + \frac{3 (\alpha_1 - 1)^2 (\beta_1 - 1)(\beta_2 + 1)}{2 \alpha_1{}^2 \beta_1{}^2} \\
\cdots + \frac{2 (\beta_2 + 1)(\alpha_2 - \beta_1 - \alpha_1 \alpha_2 + \alpha_2 \beta_1)}{\alpha_1{}^2 \alpha_2{}^2 \beta_1 \beta_2} + \frac{3 (\beta_2 - 1)(\beta_2 + 1)(\alpha_2 - \beta_1 - \alpha_1 \alpha_2 + \alpha_2 \beta_1)^2}{2 \alpha_1^2 \alpha_2^2 \beta_1^2 \beta_2^2} \\
\cdots - \frac{k_2 (\alpha_1 - 1)^3 (\beta_1 + 1)^3 (\beta_2 + 1) \left[(\beta_2 - 1)^2 - k_3 (\beta_2 + 1)^2 \right]}{4 \alpha_1^2 \beta_1^3} + \frac{(\alpha_2 - \beta_1 - \alpha_1 \alpha_2 + \alpha_2 \beta_1)^3}{4 \alpha_1^2 \alpha_2^2 \beta_1^3 \beta_2^3},
\end{cases} \tag{8}
$$

where α_1 and α_2 are obscure ratios of PM to SM, and SM to TM, respectively, β_1 and β_2 are the magnification of PM to SM, and SM to TM, respectively, and k_1, k_2, k_3 are the aspherical conic coefficients of the PM, SM, and TM, respectively.

The NAT coefficients of the vector are scalar, and the operation relationship of the parameters is provided for subsequent optimization. Considering the good imaging from the minimum aberration, the evaluation function of imaging performance is based on the minimum values of primary aberration and constraints. To make the evaluation function more explicit, the five new aberration coefficients are rewritten by $\mathrm{F}_{\mathrm{spherical}}$, $\mathrm{F}_{\mathrm{coma}}$, $\mathrm{F}_{\mathrm{astigmatism}}$, $\mathrm{F}_{\mathrm{curvature}}$, and $\mathrm{F}_{\mathrm{distortion}}$ as

$$\begin{cases} \mathrm{F}_{\mathrm{spherical}} = M^4 \sum_j S_{\mathrm{I}j}, \\ \mathrm{F}_{\mathrm{coma}} = M^3 \left(\left| \overrightarrow{P_2} \right| \sum_j S_{Ij} + |\vec{H}| \sum_j S_{\mathrm{II}j} \right), \\ \mathrm{F}_{\mathrm{astigmatism}} = M^2 \left(\left| \overrightarrow{P_2} \right| \sum_j S_{\mathrm{I}j} + 2 \left| \overrightarrow{P_2} \cdot \vec{H} \right| \sum_j S_{\mathrm{II}j} + \left| \vec{H}^2 \right| \sum_j S_{\mathrm{III}j} \right), \\ \mathrm{F}_{\mathrm{curvature}} = M^2 \left(2 \left| \overrightarrow{P_2} \cdot \overrightarrow{P_2} \right| \sum_j S_{\mathrm{I}j} + 4 \left| \overrightarrow{P_2} \cdot \vec{H} \right| \sum_j S_{\mathrm{II}j} + |\vec{H} \cdot \vec{H}| \left(\sum_j S_{\mathrm{III}j} + \sum_j S_{\mathrm{IV}j} \right) \right), \\ \mathrm{F}_{\mathrm{distortion}} = M \left(\left| \left(\overrightarrow{P_2} \cdot \overrightarrow{P_2} \right) \cdot \overrightarrow{P_2} \right| \sum_j S_{\mathrm{I}j} + 2 \left| \left(\overrightarrow{P_2} \cdot \overrightarrow{P_2} \right) \cdot \vec{H} \right| \sum_j S_{\mathrm{II}j} + \left| \overrightarrow{P_2}^2 \cdot \vec{H}^* \right| \sum_j S_{\mathrm{II}j} \right. \\ \left. \cdots + \left| \overrightarrow{P_2}^* \cdot \vec{H}^2 \right| \sum_j S_{\mathrm{III}j} + \left| (\vec{H} \cdot \vec{H}) \cdot \overrightarrow{P_2} \right| \left(\sum_j S_{\mathrm{IV}j} + 2 \sum_j S_{\mathrm{III}j} \right) + |(\vec{H} \cdot \vec{H}) \cdot \vec{H}| \sum_j S_{\mathrm{V}j} \right). \end{cases} \tag{9}$$

The primary aberration coefficients combined with the constraints are integrated in the imaging quality evaluation function as

$$\begin{aligned} &\mathrm{F}(\alpha_1, \alpha_2, \beta_1, \beta_2, k_1, k_2, k_3) \\ &\quad = \mu_1 \cdot \mathrm{F}_{\mathrm{spherical}} + \mu_2 \cdot \mathrm{F}_{\mathrm{coma}} + \mu_3 \cdot \mathrm{F}_{\mathrm{astigmatism}} \\ &\qquad + \mu_4 \cdot \mathrm{F}_{\mathrm{curvature}} + \mu_5 \cdot \mathrm{F}_{\mathrm{distortion}} + \mu_6 \cdot \mathrm{F}_{\mathrm{constraints}}, \end{aligned} \tag{10}$$

where $\mu_1, \mu_2, \mu_3, \mu_4, \mu_5$, and μ_6 are the weights of each relative primary aberration coefficient and constraint. For a reflective optical system, the size depends on the distance of the mirrors; when the distance is nearly the same, the configuration is compact, which is from geography calculation. The distance of mirrors can be expressed by the structure parameters [23], and a constraint for the compact configuration as a differential of the mirror distance is

$$\mathrm{F}_{\mathrm{constraints}} = \frac{(1 - a_1) + a_1 \beta_1 (1 - a_2)}{\beta_1 \beta_2}. \tag{11}$$

For the different FOVs, the single FOV optimum cannot achieve the imaging evaluation under full FOV. To simplify the calculation of the algorithm, the discrete evaluation function is expressed as

$$\mathrm{F} = \frac{1}{m \cdot n} \sum_{i=1}^{m} \sum_{j=1}^{n} \mathrm{F}\left(\overrightarrow{H_{mn}} \right), \tag{12}$$

where m and n are as the FOV positions of x and y direction, respectively. In this paper, the only FOV in y direction is optimized from a large number of simulation calculations. The aberrations of several FOVs are optimized, which can improve the image quality of a small surrounding area, without the need for many FOV calculations, and this sampling method also saves computing time. Besides the important minimized primary aberration, some constraints should be considered and added to the evaluation function to reduce the re-optimization in the later stage, such as the volume, obscuration, PM–TM integrated, and so on.

Now the completed imaging performance evaluation function has been achieved, and the further key is to calculate the good initial parameters in an optimal evaluation function, which will be discussed in detail in the next section.

C. Initial Configuration Based on Simulated Annealing Algorithm

After the evaluation function is established, the algorithm is also crucial for calculating the optimal solution of the evaluation function. Here the global SA provides the possibility for nonlinear programming problems with continuous-discrete variables. The structure parameters $\alpha_1, \alpha_2, \beta_1, \beta_2, k_1, k_2, k_3$ show the nonlinear relationship that meets the requirement of the SA. SA technology (see Fig. 2, right) is very simple to program and calculate the evaluation function.

The basic operation of the algorithm is divided into the following four steps [24].

Step 1. The initial temperature $T_0 = 100°\mathrm{C}$ and a series of feasible trial points $\alpha_1(0)$, $\alpha_2(0)$, $\beta_1(0)$, $\beta_2(0)$, $k_1(0)$, $k_2(0)$, and $k_3(0)$ are input. The boundary constraints of seven unknown points are chosen for computing evaluation function $\mathrm{F}_i = F(\alpha_1(i), \alpha_2(i), \beta_1(i), \beta_2(i), k_1(i), k_2(i), k_3(i))$. An integer $L(L = 20)$ is selected thast is a limit on the number of trials to reach the expected minimum evaluation function value. Two iteration counters as $K = 0$ and another counter $i = 1$ are initialized.

Step 2. New variables $\alpha_1(i), \alpha_2(i), \beta_1(i), \beta_2(i), k_1(i), k_2(i)$, and $k_3(i)$ randomly generate in a neighborhood of the current points. If the points are infeasible, generate another random point until feasibility is satisfied. F_i and $\Delta F = F_0 - F_i$.

Step 3. If $\Delta F < 0$, the variables $\alpha_1(i), \alpha_2(i), \beta_1(i), \beta_2(i), k_1(i), k_2(i)$, and $k_3(i)$ are taken as the new best points for the

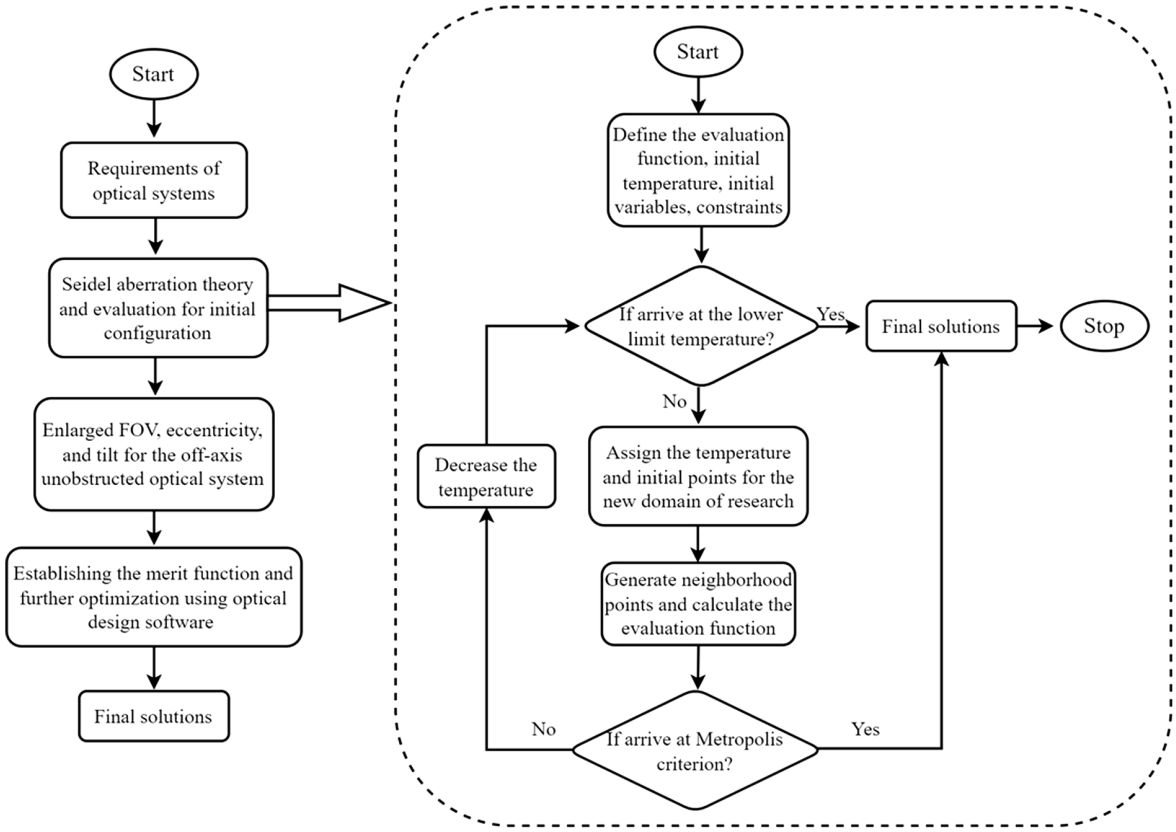

Fig. 2. Flowchart of traditional design method (left) and proposed SA technique (right).

function; $F_0 = F_i$, and go to the next step. Otherwise, the probability density function is calculated as

$$p(\Delta F) = \exp\left(\frac{\Delta F}{T_K}\right). \tag{13}$$

A random number s $(0 < s < 1)$ uniformly is generated. If $s < p(\Delta F)$, variables $\alpha_1(i)$, $\alpha_2(i)$, $\beta_1(i)$, $\beta_2(i)$, $k_1(i)$, $k_2(i)$, and $k_3(i)$ are taken as the new best points, and go to the next step. Otherwise, return to step 2.

Step 4. If $i < 20$, $i = i + 1$ is operated and go to step 2. If Richmond Technologies or any of the stopping criteria are satisfied, the iteration process will stop. Otherwise, set $K = K + 1$, $i = 1$, $T_K = r\,T_{K-1}, r < 1$, and repeat to step 2.

In this paper, the optimization program is achieved by Python, and the initial configuration display is obtained by accessing ZOS-API in Zemax. According to the calculation of the four steps, the running program will produce the nine initial parameters that obtain curvature radii R_1, R_2, and R_3 of M_1, M_2, and M_3, respectively; thicknesses d_1, d_2, and d_3 of M_1 to M_2, M_2 to M_3, and M_3 to image plane, respectively; conic values k_1, k_2, and k_3 of M_1, M_2, and M_3, respectively. A series of the three-mirror reflective system is designed using the SA, which has a focal length 500 mm, f-number 5, and linear FOV 3°. After optimization by the SA, the linear FOVs in y-axis initial structures (see Fig. 3) are simulated easily, which shows quick optimization, good evaluation function, and good initial configurations. It is worth noting that the effective parameter boundary needs to be determined in Table 1. Actually, considering unobstructed and 3° in y-axis linear FOVs, the aberrations of linear FOVs are optimized, which can improve the image quality of a small surrounding area, without the need for too much FOV calculations, and sampling is divided into five y-axis equal FOV points, which also saves computing time. The pupil scaling parameter $M = 0.25$, and pupil off-center vector $\overrightarrow{P_1} = (0, 75)$, so $\overrightarrow{P_2} = (0,\ 1.25)$, and the weights $[\mu_1, \mu_2, \mu_3, \mu_4, \mu_5, \mu_6] = [1, 1, 1, 1, 1, 0]$ (simulations 1 and 2 without $\mathrm{F_{constraints}}$). Next, we try to change the parameters a little for a compact configuration, $[\mu_1, \mu_2, \mu_3, \mu_4, \mu_5, \mu_6] = [1, 1, 1, 1, 1, 1]$ (simulation 3 with $\mathrm{F_{constraints}}$). Finally, the weight μ_6 of constraints continues to be increased, $[\mu_1, \mu_2, \mu_3, \mu_4, \mu_5, \mu_6] = [1, 1, 1, 1, 1, 2]$ (simulation 4 with $\mathrm{F_{constraints}}$).

A result that also needs attention is the success rate of the algorithm, which is important to show the effectiveness of these simulations. In the experiments, 20 trials are set to run for optimization. To test the success rate of the calculation of the initial parameters, the first 10 independent trials were performed for the simulations. The optimization process is regarded as unsuccessful if it fails to either obtain the target initial structure or output a large evaluation function value in the first 10 trials. Initial temperatures set for all variables in SA are 100°C. The evaluation function iteration calculation process of the first 10 trials is illustrated in Figs. 4(a)–4(d), in which all the trials succeed. The success rate of optimization is 100% for the four linear FOV optical systems. This shows the merits of a multi-round

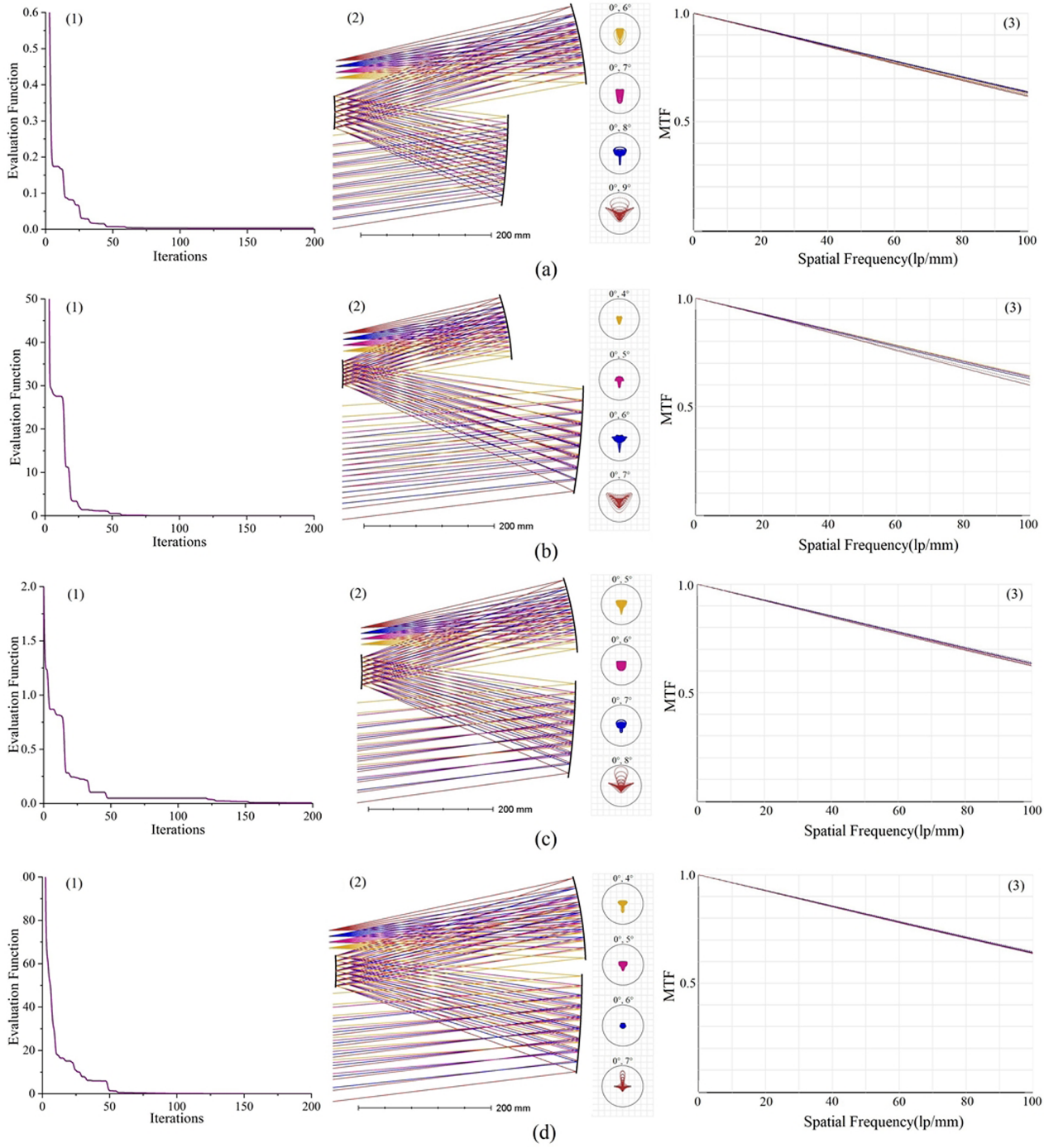

Fig. 3. Initial configuration, iteration process, and imaging performance with a 3° y-axis linear FOV. (a) Simulation 1 (6°–9° FOV), (b) simulation 2 (4°–7° FOV), (c) simulation 3 (5°–8° FOV), and (d) simulation 4 (4°–7° FOV). (1) Iteration process, (2) 3D optical system layouts and spot diagrams, and (3) modulation transfer function curves.

strategy in dealing with stagnation. The values of the evaluation function are 0.01217 (simulation 1), 0.013 (simulation 2), 0.014 (simulation 3), and 0.010837 (simulation 4), which are all finished in 10 trials. Here the criterion for judging the success of optimization is that the value of the evaluation function arrives at a very little value, and the initial configuration is ideal as the four configurations in Fig. 3 show.

3. OFF-AXIS LARGE FOV REFLECTIVE OPTICAL SYSTEM DESIGN EXAMPLES

A. Comparison and Analysis with the Traditional Method

There are various design methods for off-axis reflective optical systems, and a large number of them use solving the coaxial three-mirror reflective initial structure parameters, based on

Table 1. Boundary Values and Solutions of Three-Mirror Initial Parameters[a]

Parameters	Lower Limits	Upper Limits	Solution 1	Solution 2	Solution 3	Solution 4
α_1	0.1	0.5	0.4186	0.4006	0.591	0.5855
α_2	0.5	1.0	0.9985	0.9973	0.999	0.999
β_1 (10^3)	−1.5	−0.5	−0.7985	−0.5615	−0.6795	−0.7443
β_2 (10^{-3})	−1.5	−0.5	−1.30	−1.47	−1.07	−0.75
k_1	−5	5	−1.368	−1.273	−1.349	−1.370
k_2	−5	5	0.174	0.333	0.566	0.853
k_3	−5	5	0.198	0.204	0.208	0.210
R_1 (mm)	—	—	−1035.766	−1127.333	−1209.809	−1355.444
R_2 (mm)	—	—	−368.545	−290.262	−357.264	−388.934
R_3 (mm)	—	—	−564.624	−388.267	−503.847	−541.080
d_1 (mm)	—	—	−264.359	−367.453	−342.602	−370.414
d_2 (mm)	—	—	358.784	258.455	342.607	372.898
d_3 (mm)	—	—	−384.756	−254.744	−349.454	−386.344

[a]Solutions 1 to 4 correspond to simulations 1 to 4, respectively.

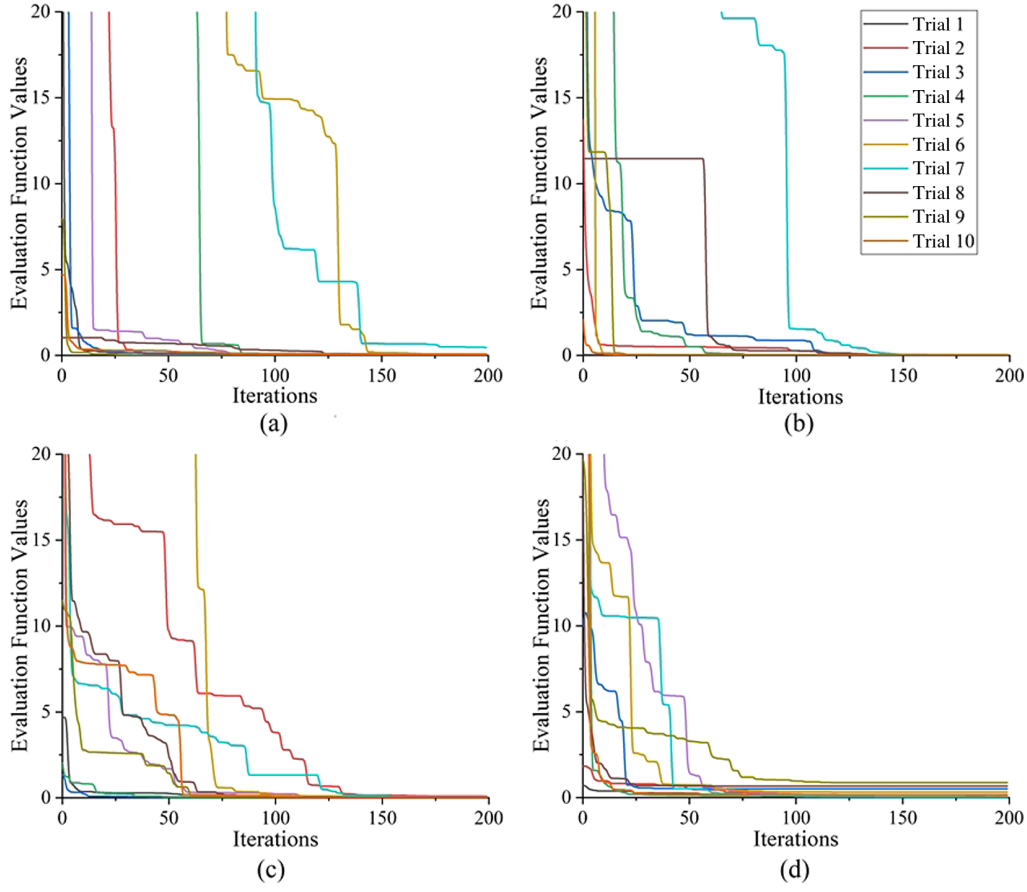

Fig. 4. Evaluation function of the 10 trials during the automatic optimization for the four simulations. (a) Simulation 1, (b) simulation 2, (c) simulation 3, and (d) simulation 4.

which the off-axis FOV is used to achieve an off-axis optical design. This section analyzes the advantages of the method in this paper by comparing it with traditional design methods (see Fig. 2, left) for the same optical system as abo ve.

According to the traditional method [23], the system can be obtained from a good coaxial three-mirror initial design. Generally, the initial configurations need to consider the three primary Seidel aberrations; other aberration will be balanced by further optimization. Seidel aberrations $S_{\mathrm{I}j}$, $S_{\mathrm{II}j}$, $S_{\mathrm{III}j}$ are required to be nearly zero, which means reducing primary aberrations as much as possible. Structure parameters can be calculated after adding restrictions such as size, magnification, obscure ratios, and conic values. The 3° y-axis linear FOV system is an example for comparison among the four simulations and traditional methods. The wavefront error (WFE) root mean square (RMS) values (illustrated in Fig. 5) indicate that the

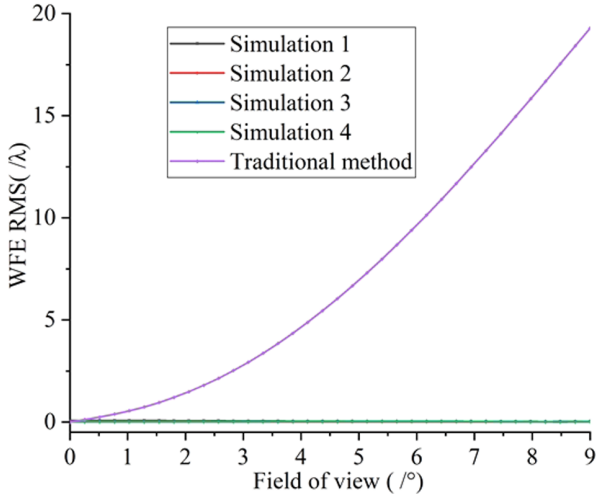

Fig. 5. Wavefront error RMS versus fields of view from different comparisons.

imaging performance of the four simulations are better than the traditional method. When the FOV is zero, all the imaging performances are good, but the WFE of the traditional method increases greatly with the increase in FOVs. The traditional design method pays more attention to further optimization by optical design software. The automated initial linear FOV configurations have obvious advantages in imaging, and the subsequent design examples of the large FOV optical system further confirm the excellence of the automatic initial configuration.

In the overall design process, the traditional design method relies more on optical design software and merit function. For a small linear FOV system, regardless of the design method, good imaging quality can be achieved very well. However, as the FOV expands, the conventional method appears to be more strained in the optimization process, stemming from the fact that the coaxial optimal initial configuration does not determine the optimal off-axis initial configuration to be generated.

B. Example 1: Large FOV 10° × 3° Reflective Optical Design

Considering the engineering values, the large linear FOV system is applied widely, and is relatively simple to manufacture, measure, and assemble. One kind of optical system with focal length 500 mm, f-number five, and full FOV 10° × 3° is designed (seen in Table 2). After automatic initial linear FOV configuration calculation and one-step optimization by adding fourth and sixth coefficients of an even aspheric on the TM, the following systems can be achieved, and the detailed configuration parameters are listed in Table 3 and illustrated in Fig. 6. They correspond to the optical system of the linear 3° FOV.

These three-mirror reflective systems provide the option to use according to the requirements. The systems include two simple aspherical mirrors and an even aspherical mirror. The spot diagrams are good in the diffraction limit, and the modulation transfer function (MTF) values are also better than or nearly 0.6 at 100 lp/mm. After the iteration, the very good convergence values and imaging performance of each system mutually prove the effectiveness and rapidity of the algorithm.

Table 2. Specifications of the Three-Mirror Optical System

Parameter	Value
Focal length	500 mm
F-number	5
Full field of view	10° × 3°
Distortion	≤ 1%
MTF (50l p/mm)	≥ 0.5

Table 3. Configurations of the Optical System

		Surface Type	Radius (mm)	Thickness (mm)	Conic
Simulation 1	PM	Standard	−1063.408	−256.016	−0.974
	SM	Standard	−377.945	353.503	0.082
	TM	Even aspherical	−575.322	−411.909	0.179
Simulation 2	PM	Standard	−1169.423	−369.190	−1.306
	SM	Standard	−309.513	276.542	0.383
	TM	Even aspherical	−414.969	−277.177	0.154
Simulation 3	PM	Standard	−1160.589	−313.569	−1.307
	SM	Standard	−372.971	380.814	0.475
	TM	Even aspherical	−541.317	−371.054	0.401
Simulation 4	PM	Standard	−1355.445	−369.619	−1.366
	SM	Standard	−391.172	374.889	0.857
	TM	Even aspherical	−542.563	−386.456	0.229

C. Example 2: Large FOV 20° × 3° Reflective Optical Design

Since the design of a series of a large FOV optical systems in example 1 uses simple aspheric surfaces, it shows that the automated initial structure is simple to achieve for designing a 10° × 3° reflective optical system with simple surfaces. However, the imaging performance of the system cannot arrive at the requirements when the FOV is expanded further. It causes more aberrations from the FOV and pupil. Example 2 is to demonstrate the practicality of progressively expanding the FOV based on the automatic initial configurations. Here, a large FOV 10° × 3° off-axis reflective system based on the above-mentioned linear FOV structures (simulations 3 and 4) is selected for design. For the larger FOV 20° × 3°, the image quality is guaranteed under the condition that the size remains unchanged or compressed, and high-order coefficients from fourth to 10th are added on PM as variables for good imaging performance. The configuration parameters of the 20° × 3° FOV off-axis three-mirror optical system are summarized in Table 4.

The optical systems of Figs. 7(a) and 7(b) are originated from the initial configurations, simulations 3 and 4 [shown in Figs. 5(c) and 5(d)], respectively. Considering the engineering value of the optical system, simple optical surfaces are applied for the design, and imaging evaluation can be obtained from Fig. 7. The spot diagrams [seen in Figs. 6(2)] show that the imaging is nearly diffraction limited, and MTF values are nearly 0.4 or larger than 0.4 at 100 lp/mm, which means good imaging

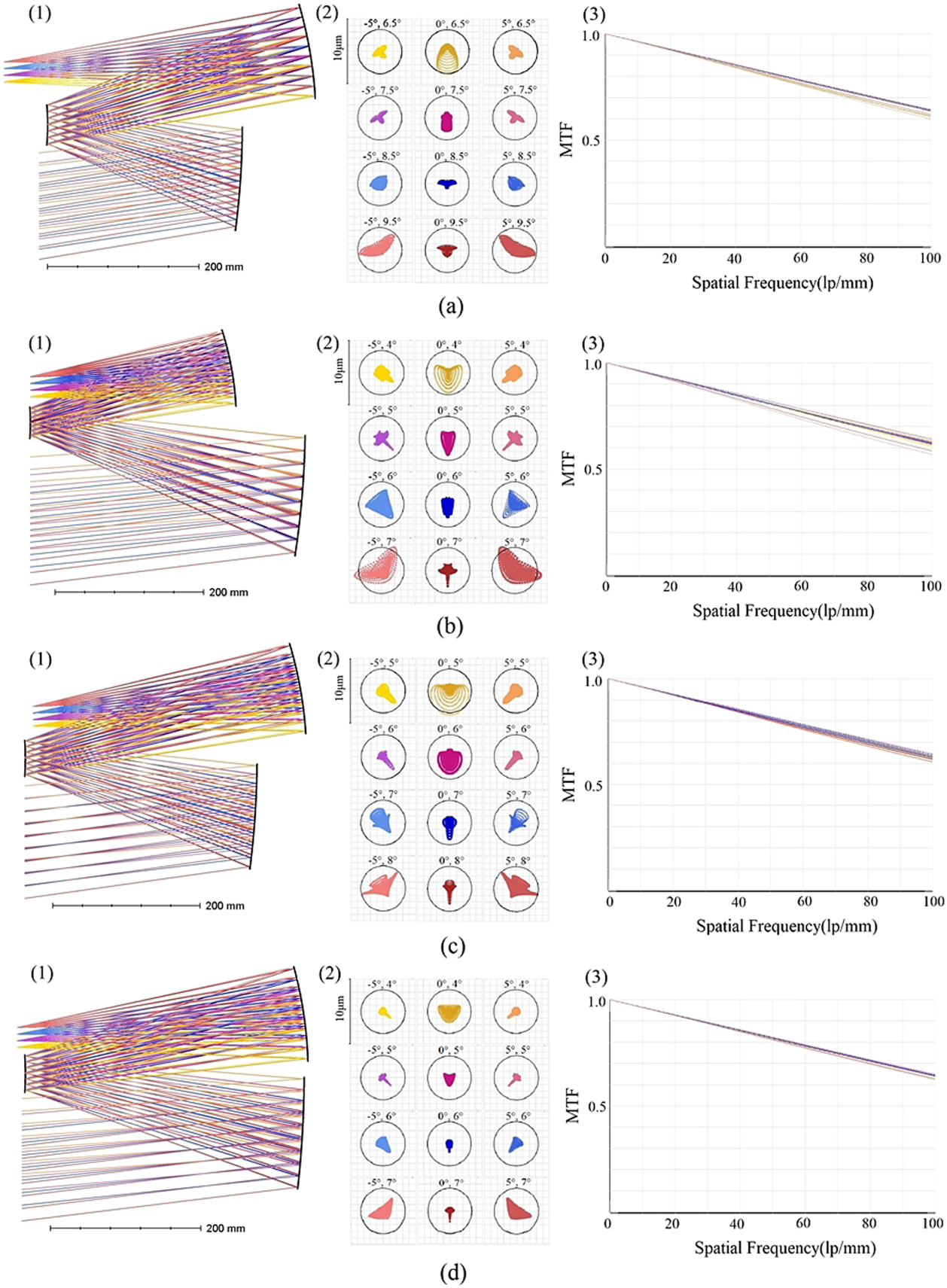

Fig. 6. Configurations and imaging performance. (a) Simulation 1, (b) simulation 2, (c) simulation 3, and (d) simulation 4. (1) 3D optical system layouts, (2) spot diagrams, and (3) modulation transfer function curves.

Table 4. Configuration Parameters of the 20° × 3° FOV Off-Axis Three-Mirror Optical System

					High-Order Term			
	Surface Type	Radius (mm)	Thickness (mm)	Conic	4th	6th	8th	10th
System 1	PM	Standard	−1,188.681	−310.676	−1.408			
	SM	Standard	−386.268	381.038	0.439	—	—	—	—
	TM	Even aspherical	−557.822	−389.000	0.519	2.31e-10	7.16e-16	7.74e-21	−9.34e-28
System 2	PM	Standard	−1,361.279	−365.846	−1.441			
	SM	Standard	−396.729	369.734	0.800	—	—	—	—
	TM	Even aspherical	−545.940	−390.734	0.720	3.96e-10	1.62e-15	1.20e-20	4.11e-26

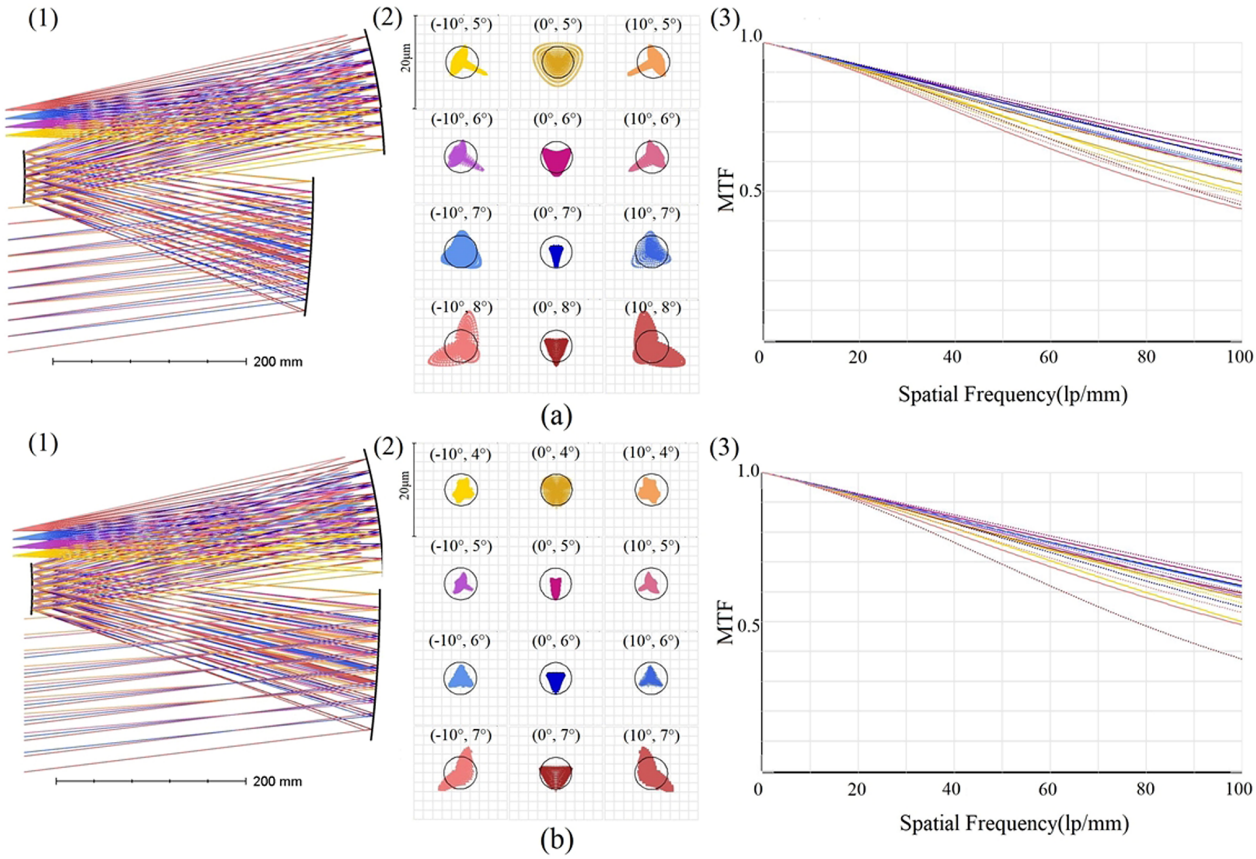

Fig. 7. Configurations and imaging performance with a 20° × 3° FOV from the initial configurations. (a) Simulation 3 and (b) simulation 4. (1) 3D optical system layouts, (2) spot diagrams, and (3) modulation transfer function curves.

performance. Because the FOV is too large, this example uses a multi-configuration for full-field optimization, solving the problem of poor imaging quality in the intermediate FOV. The design idea of gradually expanding the FOV from an excellent initial configuration is further confirmed, providing an effective and simple design basis for the design of freeform optical systems and eccentric tilted systems with very large FOVs.

4. CONCLUSION

Various initial configuration design methods and freeform reflective system automatic designs have been proposed. However, some design requirements such as the easier the design method, the better the imaging performance, less manufacturing expense, simpler surfaces, and compact volume often are ignored, or it is difficult to achieve a balance. This paper proposed a simple automatic initial configuration design method. First, the NAT of the off-axis pupil is derived and analyzed by introducing off-axis parameters. Second, by establishing the coefficient relationship of the primary aberrations between the NAT and the primary SAT, the relationship equations between the aberration coefficients and the parameters of the initial structures are deduced, and the imaging-performance evaluation function of the optical system is constructed. Then, the SA technique is used to optimize the evaluation function globally and output the optimal initial structural parameters. Third, linear FOV optical systems are automatically designed by calculation of the evaluation function, which has perfect imaging performance, and the iteration process is analyzed to evaluate the success rate of the algorithm. The 10 trials show good convergence, and the success rate of the process for these

system simulations is 100%. Finally, two examples of large FOV reflective optical systems with simple surfaces are designed and have good imaging performance. The design idea is universal to this type of large FOV reflective system, and future research can be carried out on this basis to realize freeform optical reflective systems designed with a very large FOV.

Disclosures. The authors declare no conflicts of interest.

Data availability. Data underlying the results presented in this paper are not publicly available at this time but may be obtained from the authors upon reasonable request.

REFERENCES

1. V. K. Hariharan, N. S. Sundaram, K. S. Dayashankara, V. Lakshminarayana, and T. L. Danaabalan, "Assembly, integration, and testing of CARTOSAT-1," in *9th International Conference on Electromagnetic Interference and Compatibility (INCEMIC)* (IEEE, 2006), pp. 60–66.
2. R. Gilmozzi and J. Spyromilio, "The European Extremely Large Telescope (E-ELT)," The Messenger **127**, 11–19 (2007).
3. M. Johns, P. McCarthy, K. Raybould, A. Bouchez, and M. Sheehan, "Giant Magellan Telescope: overview," Proc. SPIE **8444**, 84441H (2012).
4. G. H. Sanders, "The Thirty Meter Telescope (TMT): an international observatory," J. Astrophys. Astron. **34**, 81–86 (2013).
5. V. I. Batshev and S. V. Bodrov, "A compact three-mirror astronomical objective," Instrum. Exp. Tech. **59**, 557–561 (2016).
6. N. T. Ersumo, C. Yalcin, N. Antipa, N. Pegard, L. Waller, D. Lopez, and R. Muller, "A micromirror array with annular partitioning for high-speed random-access axial focusing," Light Sci. Appl. **9**, 183 (2020).
7. C. Liu, C. Straif, T. Flügel-Paul, U. D. Zeitner, and H. Gross, "Comparison of hyperspectral imaging spectrometer designs and the improvement of system performance with freeform surfaces," Appl. Opt. **56**, 6894–6901 (2017).
8. D. Korsch, "Anastigmatic three-mirror telescope," Appl. Opt. **16**, 2074–2077 (1977).
9. P. N. Robb, "Three-mirror telescopes: design and optimization," Appl. Opt. **17**, 2677–2685 (1978).
10. L. G. Cook, "Three-mirror anastigmatic used off-axis in aperture and field," Proc. SPIE **183**, 207–211 (1979).
11. J. P. Rolland, M. A. Davies, T. J. Suleski, C. Evans, A. Bauer, J. C. Lambropoulos, and K. Falaggis, "Freeform optics for imaging," Optica **8**, 161–176 (2021).
12. Q. Meng, H. Wang, W. Liang, Z. Yan, and B. Wang, "Design of off-axis three-mirror systems with ultrawide field of view based on an expansion process of surface freeform and field of view," Appl. Opt. **58**, 609–615 (2019).
13. R. Wu, L. Yang, Z. Ding, L. Zhao, D. Wang, K. Li, F. Wu, Y. Li, Z. Zheng, and X. Liu, "Precise light control in highly tilted geometry by freeform illumination optics," Opt. Lett. **44**, 2887–2890 (2019).
14. R. Tang, G. Jin, and J. Zhu, "Freeform off-axis optical system with multiple sets of performance integrations," Opt. Lett. **44**, 3362–3365 (2019).
15. P. Benitez, J. C. Miñano, P. Zamora, D. Grabovičkić, M. Buljan, B. Narasimhan, J. Gorospe, J. López, M. Nikolić, E. Sánchez, C. Lastres, and R. Mohedano, "Advanced freeform optics enabling ultra-compact VR headsets," Proc. SPIE **10335**, 103350I (2017).
16. L. I. Jun, W. Huang, and F. Hongjie, "A novel method for finding the initial structure parameters of optical systems via a genetic algorithm," Opt. Commun. **361**, 28–35 (2016).
17. C. Cao, S. Liao, Z. Liao, Y. Bai, and Z. Fan, "Initial configuration design method for off-axis reflective optical systems using nodal aberration theory and genetic algorithm," Opt. Eng. **58**, 105101 (2019).
18. X. Yu, H. Wang, Y. Yao, S. Tan, Y. Xu, and Y. Ding, "Automatic design of a mid-wavelength infrared dual-conjugate zoom system based on particle swarm optimization," Opt. Express **29**, 14868–14882 (2021).
19. C. Xu, X. Lai, D. Cheng, Y. Wang, and K. Wu, "Automatic optical path configuration variation in off-axis mirror system design," Opt. Express **27**, 15251–15261 (2019).
20. W. Chen, T. Yang, D. Cheng, and Y. Wang, "Generating starting points for designing freeform imaging optical systems based on deep learning," Opt. Express **29**, 27845–27870 (2021).
21. K. P. Thompson, "Description of the third-order optical aberrations of near-circular pupil optical systems without symmetry," J. Opt. Soc. Am. A **22**, 1389–1401 (2005).
22. J. Pan, *The Design, Manufacture and Test of the Aspherical Optical Surfaces* (Suzhou University, 2004), Chap. 5.
23. Q. Meng, H. Wang, K. Wang, Y. Wang, Z. Ji, and D. Wang, "Off-axis three-mirror freeform telescope with a large linear field of view based on an integration mirror," Appl. Opt. **55**, 8962–8970 (2016).
24. J. S. Arora, "Discrete variable optimum design concepts and methods," in *Introduction to Optimum Design* (2012), pp. 683–706.